

ROS enhancement by silicon nanoparticles in X-ray irradiated aqueous suspensions and in glioma C6 cells

Pedro M. David Gara · Natalia I. Garabano ·
Manuel J. Llansola Portoles · M. Sergio Moreno ·
Diego Dodat · Oscar R. Casas · Mónica C. Gonzalez ·
Mónica L. Kotler

Received: 10 February 2011 / Accepted: 14 January 2012
© Springer Science+Business Media B.V. 2012

Abstract The capability of silicon nanoparticles to increase the yield of reactive species upon 4 MeV X-ray irradiation of aqueous suspensions and C6 glioma cell cultures was investigated. ROS generation was detected and quantified using several specific probes. The particles were characterized by FTIR, XPS, TEM, DLS, luminescence, and adsorption spectroscopy before and after irradiation to evaluate the effect of high energy radiation on their structure. The

total concentration of $O_2^{\bullet-}/HO_2^{\bullet}$, HO^{\bullet} , and H_2O_2 generated upon 4-MeV X-ray irradiation of 6.4 μM silicon nanoparticle aqueous suspensions were on the order of 10 μM per Gy, ten times higher than that obtained in similar experiments but in the absence of particles. Cytotoxic 1O_2 was generated only in irradiation experiments containing the particles. The particle surface became oxidized to SiO_2 and the luminescence yield reduced with the irradiation dose. Changes in the surface morphology did not affect, within the experimental error, the yields of ROS generated per Gy. X-ray irradiation of glioma C6 cell cultures with incorporated silicon nanoparticles showed a marked production of ROS proportional to the radiation dose received. In the absence of nanoparticles, the cells showed no irradiation-enhanced ROS generation. The obtained results indicate that silicon nanoparticles of <5 nm size have the potential to be used as radiosensitizers for improving the outcomes of cancer radiotherapy. Their capability of producing 1O_2 upon X-ray irradiation opens novel approaches in the design of therapy strategies.

Electronic supplementary material The online version of this article (doi:10.1007/s11051-012-0741-8) contains supplementary material, which is available to authorized users.

P. M. David Gara · D. Dodat · O. R. Casas
CITOMA, Fundación Avanzar, Instituto de Terapia
Radiante S.A., CIO La Plata, Calle 60 Nro. 480 (1900), La
Plata, Argentina

P. M. David Gara · M. J. Llansola Portoles ·
M. C. Gonzalez (✉)
INIFTA, Departamento de Química, Facultad de Ciencias
Exactas, UNLP, CC16 Suc. 4 (1900), La Plata, Argentina
e-mail: gonzalez@inifta.unlp.edu.ar

N. I. Garabano · M. L. Kotler (✉)
Departamento de Química Biológica, Facultad de
Ciencias Exactas y Naturales, UBA, University of Buenos
Aires, Intendente Güiraldes 2160, C1428EGA Buenos
Aires, Argentina
e-mail: kotler@qb.fcen.uba.ar

M. S. Moreno
Centro Atómico Bariloche, 8400 San Carlos de
Bariloche, Argentina

Keywords Silicon nanoparticles · Radiotherapy ·
Glioma C6 cells · ROS · X-rays · Singlet molecular
oxygen

Introduction

Despite the considerable progress made in cancer therapy, ionizing radiation is still the most widespread

and efficient treatment for solid tumors (Hall and Giaccia 2006). In particular, the prognosis for patients with malignant glioma, the most common type of brain tumor in adults, changed little in the last decades and this tumor remains resistant to current treatment strategies (Soffietti et al. 2007). Glioma requires high special accuracy in the delivery of the ionizing radiation to minimize damage to surrounding tissues (Park et al. 2006).

Nanomaterials used as radiosensitizers are known to increase the radiotherapeutic efficiency by selectively scattering and/or absorbing X- and γ -rays causing localized damage to DNA and other targeted organelles of tumor cells (Zhang et al. 2009; Mitrasi-novic and Mihajlovic 2008). Significant synergistic effects result from the use of γ -radiation on nanosized systems far beyond the effects observed in bulk materials (Carter et al. 2007). The targeted localized damage due to the higher density of solid particles, their capability to produce reactive radicals upon irradiation (Seino et al. 2003; Isakovic et al. 2006; Takahashi and Misawa 2007), and the unmatched surface modification methodologies that nanoparticles offer, are key properties to take advantage of in dose enhancement strategies of cytostatic and cytolytic activities in tumor cells by ionizing radiation. For example, an enhanced cell death induced by semiconductor CdSe quantum dots and their porphyrin conjugates in combination with radiation therapy was observed compared with radiation alone (Juzenas et al. 2008; Kovalev and Fujii 2005; Yang et al. 2008; Wang et al. 2010). In this regard, there is an increased interest in the applications of semiconductor nanoparticles as radiosensitizers.

Silicon semiconductor nanoparticles of 1–5 nm size, also known as silicon quantum dots, have received great attention as they combine size-dependent photoluminescence due to quantum confinement of the exciton (Yoffe 2001), the richness of silicon surface chemistry (Kang et al. 2011), and the capacity to photosensitize singlet oxygen ($^1\text{O}_2$) and to photo-reduce O_2 , methyl viologen (Llansola Portolés et al. 2010) and metal ions as Cr^{6+} , Au^{3+} , and Ag^+ (Kang et al. 2011). Remarkable properties of silicon nanoparticles when compared to other materials are their biocompatibility, biodegradability, and tunable surface derivatization for drug delivery (Erogbogbo et al. 2011). In vivo assays indicate that silicon nanoparticles are metabolized and eliminated from the body in

relatively short times (Park et al. 2009). These last observations are of importance since metabolic oxidation of silicon to SiO_2 would potentiate the particle toxicity with time (Chen and Mikecz 2005).

Bulk silicon semiconductor has long been used as an X-ray detector material due to its high density and low energy requirement (3.62 eV at room temperature) for the formation of an electron–hole pair (exciton) necessary for the measurement of radiation (Knoll 1989; Bertolini and Coche 1968). Since excitons formed upon UV–vis irradiation of silicon quantum dots may undergo energy and charge-transfer processes with surface-adsorbed O_2 to generate $^1\text{O}_2$ and $\text{O}_2^{\bullet-}$ (Llansola Portolés et al. 2010), X-ray irradiation of silicon nanoparticles is also expected to yield reactive oxygen species (ROS). We have therefore explored the potential ability of commercially available silicon nanoparticles, Si-NPC, and laboratory synthesized 2-methyl 2-propenoic acid methyl ester derivatized silicon nanoparticles, MMASi-NP (Llansola Portolés et al. 2009), to enhance ROS generation upon X-ray irradiation employing clinically relevant dose rates. Concomitant changes in the surface chemistry and optical properties were observed by FTIR, XPS, and luminescence techniques. ROS generation in tumor cells was also addressed. The work described here constitutes a first approach in the development of silicon nanoparticles as ROS enhancers for radiotherapy.

Results and discussion

Particle characterization and modification by X-ray irradiation

The morphology and mean size distribution of silicon nanoparticles were studied by transmission electron microscopy (TEM) and dynamic light scattering (DLS). MMASi-NP TEM micrographs show a narrow Gaussian distribution with an average particle diameter of 3 ± 1 nm (see Llansola Portolés et al. 2009). The DLS experiments of these particles show an average hydrodynamic radio of 2.4 ± 0.15 nm and a polydispersity of 0.2, see ESM 1. Both experiments show a size dispersion of ~ 1 nm for MMASi-NP, in agreement with that measured by fluorescence correlation spectroscopy (Llansola Portolés et al. 2009). The ~ 1.8 nm difference in the particle size measured

by DLS and TEM suggest little aggregation of MMASi-NP in suspension and may be attributed to a difference in the physical properties involved in each experiment (hydrodynamic diffusion vs. projected area) (Hackley and Clogston 2007).

On the other hand, Si-NPC TEM micrographs show a broad size distribution in the range from 3 to 90 nm which follows a LogNormal distribution centered at 14 nm (see ESM 2). DLS measurements yield a hydrodynamic radius of 289 nm with a polydispersoid of 0.3. The large differences in the size distributions obtained from TEM and DLS measurements reflect the presence of clusters of particles. In fact, static light scattering measurements yield a fractal dimension of 1.92, supporting the presence of fractal-like aggregates composed of sintered spherical primary particles as observed by TEM (Schärfl 2007).

The FTIR spectra of water-exposed MMASi-NP (see Fig. 1) and Si-NPC show intense Si–OH stretching modes at $3,400\text{ cm}^{-1}$, less intense absorption at $1,630\text{--}1,650$ and 800 cm^{-1} also assigned to Si–OH groups, and Si–O–Si vibrations absorbing at $1,050\text{--}1,100\text{ cm}^{-1}$. The later observations and the absence of Si–H stretching modes in the wavelength

range $2,100\text{--}2,200\text{ cm}^{-1}$ (Kravets et al. 2005), clearly indicate an oxidized particle surface. Particle exposition to water was reported to cause hydroxylation of the surface, as Si–OH vibrations are absent in the FTIR spectrum of freshly synthesized particles (Llansola Portolés et al. 2010). MMASi-NP spectrum also shows characteristic peaks due to C–H stretching of CH_3 ($2,920$ and $2,850\text{ cm}^{-1}$) and C=O stretching in esters ($1,724\text{ cm}^{-1}$), attributed to the covalently attached methyl ester linkers to the surface (Llansola Portolés et al. 2009, 2010).

The FTIR spectra of X-ray irradiated MMASi-NP (see Fig. 1) show increasing absorption due to Si–OH stretching modes and Si–O–Si vibrations with increasing doses. However, absorption bands due to C–H stretching of CH_3 groups are not significantly modified by X-ray irradiation up to 3 Gy. These observations suggest that X-rays preferentially oxidize surface silicon to silanol and siloxane functionalities rather than the organic groups attached to the surface. An increased surface oxidation with the irradiation dose is also observed for Si-NPC.

The photoluminescence spectrum of MMASi-NP aqueous suspensions shows emission with maximum intensity at 425 nm (50 nm FWHM) upon excitation in the range from 260 to 370 nm, as shown in Fig. 2. The emission spectrum does not change with the excitation light, as expected for a highly homogeneous size distribution of particles (Llansola Portolés et al. 2009). On the other hand, Si-NPC shows a broad emission spectrum in the wavelength range from 350 to 550 nm upon excitation in the 220–320 nm range. The maximum emission strongly depends on the excitation wavelength, as shown in Fig. 2 inset, as expected for the excitation of different size nanoparticle populations. Anisotropy correlation luminescence lifetimes experiments indicate that luminescent nanoparticles show a mean particle size of 2.4 nm (see ESM 3). Therefore, due to the broad size distribution of Si-NPC, only a small fraction of Si-NPC is responsible for the observed luminescence.

The shape of the emission spectrum of MMASi-NP and that of Si-NPC are maintained after X-ray irradiation of the particles. However, the total emission intensity significantly increases for low irradiation doses and decreases for the larger doses as shown in Fig. 1 inset.

The XPS spectrum obtained for MMASi-NP shows signals in the Si2p region (see Fig. 3) which strongly

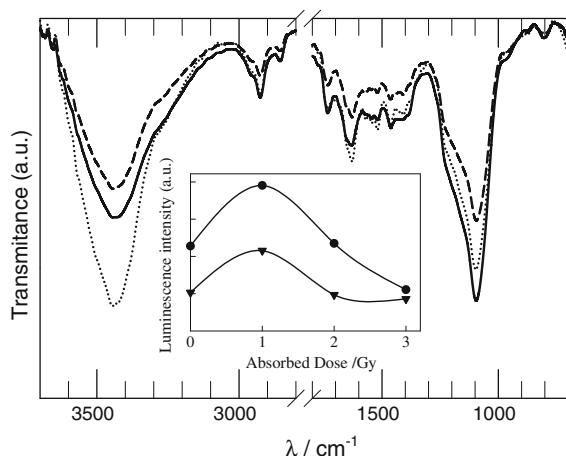


Fig. 1 Effect of ionizing radiation on the FTIR spectrum and luminescence of the particles. FTIR spectrum of KBr pellets obtained from 0.50 g/L MMASi-NP aqueous suspensions without irradiation (dashed line) and irradiated with 2 and 3 Gy (solid and dotted lines, respectively). Inset Total luminescence intensity of X-ray irradiated aqueous suspensions containing 0.50 g/L of either Si-NPC (triangle) or MMASi-NP (circle) as a function of the irradiation dose. Commercial nanoparticles were excited at 320 nm and laboratory-synthesized at 360 nm

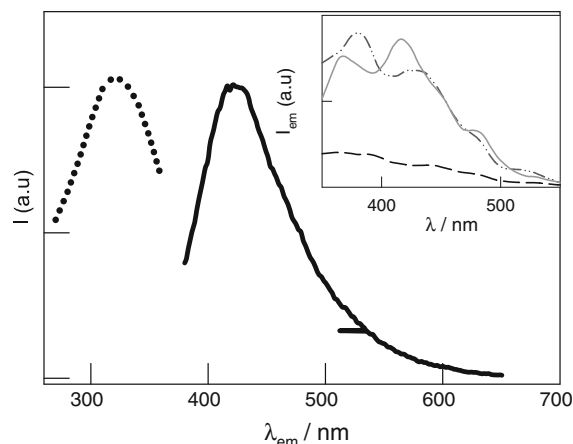


Fig. 2 Excitation and luminescence spectrum of the particles. Excitation (*dotted curve*) and luminescence spectrum (*full line*) of a 0.50 g/L MMASi-NP aqueous suspension. *Inset* Emission spectrum of a 0.10 g/L Si-NPC aqueous suspensions obtained at 300 (*solid line*), 320 (*dashed-dotted line*), and 330 nm (*dashed line*) excitation wavelength, respectively

depend on the irradiation dose. The signals can be deconvoluted into five peaks located at 103.6, 102.7, 101.4, 100.8, and 99.8 eV (see ESM 4 for deconvoluted peaks). According to the electronegativities of Si, O, and C, these five peaks can be attributed to a tetrahedral configuration with unique Si2p binding energy depending on the number of oxygen, carbon, and hydrogen atoms in the coordination shell. The binding energies may therefore be attributed to SiO₂ structure (103.6 eV), to silicon coordinated to four and two oxygen atoms (Si(OH)₄, 102.7 eV, and Si(OH)₂, 101.4 eV, respectively), to ≡Si-C≡ as in C-Si (100.8 eV), and to ≡Si-H (99.8 eV) coordination (Wang et al. 1995; Ouyang et al. 2000; Propst and Kohl 1994; Yang et al. 2001).

The nature of the changes in the silicon configuration after X-ray irradiation can therefore be monitored through analysis of the Si2p binding energy. An increase of Si(OH)₄ surface centers at the expense of >Si=O and >Si(OH)₂ surface groups, seems to take place at doses of 1 Gy, while mainly oxidation of the surface to SiO₂ is the net process at the larger doses. The generation of Si(OH)₄ centers may be related to the increased hydroxylation and siloxane bond formation of the surface of the particles. Within the experimental error, Si-C bonds seem not to be affected by X-ray radiation, in agreement with FTIR observations.

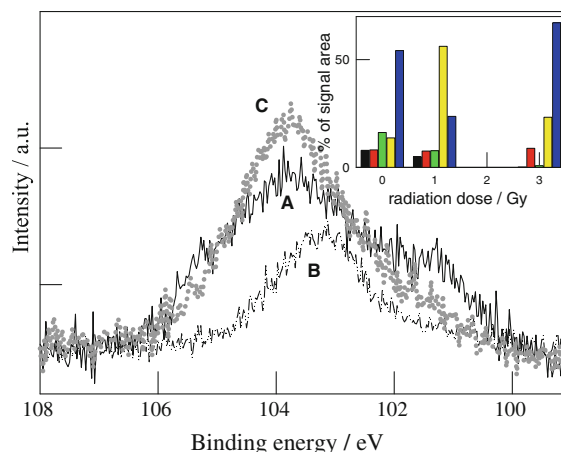


Fig. 3 Effect of ionizing radiation on the XPS spectrum. Si2p XPS peaks observed for MMASi-NP before irradiation (A) and after 1 Gy (B) and 3 Gy (C) irradiation. *Inset* Peak relative percentage as a function of the irradiation dose. SiO₂ (blue), Si(OH)₄ (yellow), >Si(OH)₂ (green), ≡Si-C≡ (red) and ≡Si-H (black) coordination

The UV-vis absorption spectrum of aqueous suspensions of MMASi-NP, show an absorption onset at about 380 nm extending towards the UV, also showing small changes with the irradiation dose (see ESM 5). Surface functionalization with organic molecules is reported not to introduce significant changes in the spectrum of the silicon particles (Takahashi and Misawa 2007). Therefore, the different absorption spectrum observed for the X-ray irradiated particles may be a consequence of a more oxidized silicon network. The variation in the luminescence intensity of MMASi-NP and Si-NPC with increasing X-ray dose may also be a consequence of the oxidation of the particle structure. The latter observations are in agreement with recent publications showing the oxidation of silicon and porous silicon under 10 keV X-ray irradiation (Ryckman et al. 2010).

ROS generation by X-ray irradiation of nanoparticle aqueous suspensions

Hydrated electrons (e_{aq}^-), H atoms, and HO• radicals are the main reactive species generated upon irradiation of water with high energy X-rays. In air-saturated solutions, e_{aq}^- and H atoms are efficiently scavenged by O₂ with rate constants of 1.9×10^{10} and $1.2 \times 10^{10} \text{ M}^{-1} \text{ s}^{-1}$, respectively, to yield O₂•⁻/HO₂• radicals (Ross et al. 1998). Hydrogen peroxide

is a secondary species formed after the recombination of either HO^\bullet or $\text{O}_2^{\bullet-}/\text{HO}_2^\bullet$. Therefore, HO^\bullet , $\text{O}_2^{\bullet-}/\text{HO}_2^\bullet$, and H_2O_2 are the main reactive species available to initiate the depletion of $\leq 1 \times 10^{-4}$ M of added scavengers in air saturated solutions. However, considering that MMASi-NP are reported to yield $^1\text{O}_2$ upon UV-visible irradiation (Llansola Portolés et al. 2010), the possible generation of $^1\text{O}_2$ upon X-ray irradiation of nanoparticles suspensions also needs to be evaluated.

To determine the generation of ROS, X-ray irradiation experiments were conducted in the presence of phenol (PhOH), furfuryl alcohol (FFA), and histidine (HIS) (Kohn and Nelson 2006, Bosio et al. 2008). Despite phenol is a known scavenger of HO^\bullet radicals, and FFA and HIS are well known scavengers for $^1\text{O}_2$, they all efficiently react with HO^\bullet radicals and with different efficiency with $^1\text{O}_2$ and $\text{O}_2^{\bullet-}$, as depicted in ESM 6. In fact, quinones and dihydroxybenzenes identified among the reaction products formed after X-ray irradiation of MMASi-NP suspensions containing phenol could arise from the probe reaction with either HO^\bullet , $^1\text{O}_2$, or $\text{O}_2^{\bullet-}$.

Figure 4 shows a linear dependence of the relative scavenger concentration remaining in solution with the irradiation dose received. Under otherwise identical conditions, all the scavengers are more efficiently depleted in irradiation experiments performed in the presence of nanoparticles than in their absence. Assuming that each molecule of scavenger is consumed per molecule of ROS, a lower limit estimation of the molar concentration of ROS produced per Gy delivered to the sample may be obtained from the concentration of scavenger removed, as depicted in Fig. 4 insets A and B for experiments performed in the absence and presence of MMASi-NP, respectively. Table 1 depicts the average lower limit concentration of ROS formed per X-ray dose delivered. The concentration of ROS achieved in experiments with 0.5 g/L MMASi-NP per Gy are on the order of 10 μM , while fractions of μM concentrations are observed in experiments in the absence of particles. Despite the particle surface becomes concomitantly oxidized to SiO_2 and the luminescence yield reduced with the irradiation dose (*vide supra*), ROS formation per Gy is, within the experimental error, insensitive to these changes up to 3 Gy irradiation. The obtained molar concentration of reactive species depends on the particular scavenger used for their quantification,

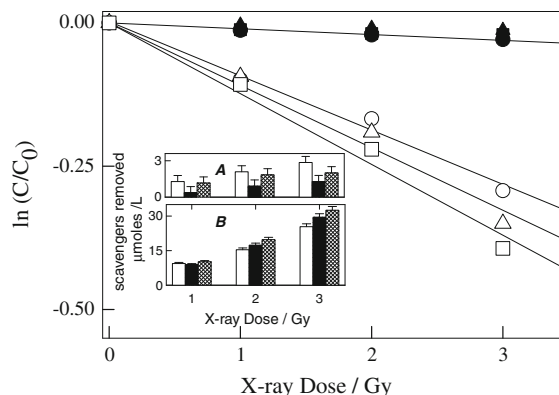


Fig. 4 ROS production in aqueous suspensions: use of PhOH, FFA, and His as scavengers. Relative scavenger concentration versus X-ray irradiation dose for solutions of 10^{-4} M PhOH (filled circle), 10^{-4} M His (filled square), 10^{-4} M FFA (filled triangle), and 0.50 g/L MMASi-NP suspensions containing 10^{-4} M PhOH (open circle), 10^{-4} M His (open square), and 10^{-4} M FFA (open triangle). The symbols size is on the order of the error in the determination of the concentration. *Inset* (A) Concentration of scavengers removed with the X-ray irradiation dose of aqueous solutions containing 10^{-4} M PhOH (white), 10^{-4} M FFA (black), and 10^{-4} M His (lined). (B) Concentration of scavengers removed with the irradiation dose of aqueous 0.50 g/L MMASi-NP suspensions containing 10^{-4} M PhOH (white), 10^{-4} M FFA (black), and 10^{-4} M His (lined)

reflecting their distinct reactivity with HO^\bullet , $^1\text{O}_2$, and $\text{O}_2^{\bullet-}$.

Despite PhOH, HIS, and FFA show similar reactivity towards HO^\bullet radicals, experiments in the absence of MMASi-NP show higher depletion rates for PhOH than for FFA and HIS. Considering that reaction with $\text{O}_2^{\bullet-}$ preferentially takes place with phenol (see ESM 6), the presence of a significant concentration of $\text{O}_2^{\bullet-}$ might further increase phenol depletion. On the other hand, X-ray irradiation experiments of aqueous suspensions of MMASi-NP evidenced somewhat higher ROS formation for HIS and FFA than for PhOH. Therefore, though the scavenging of the probes may mostly take place by reaction with HO^\bullet and $\text{O}_2^{\bullet-}$ radicals, the contribution of the reaction of HIS and FFA with $^1\text{O}_2$ cannot be discarded.

Singlet oxygen formation was further confirmed with the probe Singlet Oxygen Sensor Green, SOSG. Irradiation experiments with SOSG show fluorescence due to the $\text{SOSG}-^1\text{O}_2$ adduct only in experiments with nanoparticles. Higher fluorescence intensities were observed for the higher irradiation dose and for

Table 1 ROS enhancement by nanoparticles in irradiated aqueous suspensions

Irradiated system	Scavengers			[H ₂ O ₂]	[¹ O ₂]
	[PhOH]	[FFA]	[His]		
MMASi-NP suspensions	8.5(1)	10(1)	11(1)	1.2(0.1)	0.9(0.2)
Si-NPC suspensions	–	–	–	0.4(0.1)	0.5(0.2)
Aqueous solutions	0.95(0.2)	0.45(0.1)	0.5(0.2)	0.073(0.003)	<0.1
MMASi-NP enhancement ratio	9	22	22	16	>9
Si-NPC enhancement ratio	–	–	–	5.5	>5

Lower limit [ROS] values calculated for the different scavengers used, [H₂O₂], and [¹O₂] (all in μM units) generated per Gy of 4-MeV X-ray delivered to aqueous solutions in the presence and absence of 0.5 g/L of either MMASi-NP or Si-NPC. The ROS enhancement ratio by the nanoparticles is also shown. Estimated errors are in brackets

MMASi-NP, see Fig. 5 inset. Despite SOSG degradation initiated by reaction with HO[•] and O₂^{•−} might be of significance, formation of the fluorescent adduct is specific for ¹O₂. Therefore, the observed fluorescence unequivocally confirms ¹O₂ generation in μM concentrations, as depicted in Table 1.

Formation of μM concentrations of H₂O₂ was observed mainly in experiments in the presence of nanoparticles, increasing with the X-ray dose, as shown in Fig. 5 and depicted in Table 1. The highest concentrations were produced in experiments with MMASi-NP. Both, the recombination between O₂^{•−} and its conjugated acid (Ross et al. 1998), HO₂[•] (pK_a = 4.9), and HO[•] radical recombination may contribute to H₂O₂ generation. Therefore, the detection of μM concentrations of H₂O₂ per irradiation dose supports the generation of significant concentrations of O₂^{•−} and/or HO[•] radicals in the presence of MMASi-NP.

Commercial available particles are also able to enhance ¹O₂ and H₂O₂ formation, though their efficiency is lower than that of an equal mass of synthesized MMASi-NP, as also depicted in Fig. 5 and Table 1. The agglomerated nature of Si-NPC and/or the small fraction of these particles showing quantum confinement of the exciton (i.e., particles with size <5 nm) may be the cause for their lower ROS generation capacity.

The reported mass attenuation coefficient μ/ρ (with μ the bilinear attenuation coefficient and ρ the material density) of 4 MeV X-rays for silicon and water are 0.0340 and 0.0324 cm² g^{−1}, respectively (Hubbell and Seltzer 2010). Considering that 6.4×10^{-6} mol of 3 nm size and 2.33 g/cm³ density MMASi-NP were contained in 1 L of water, the particles contribution to

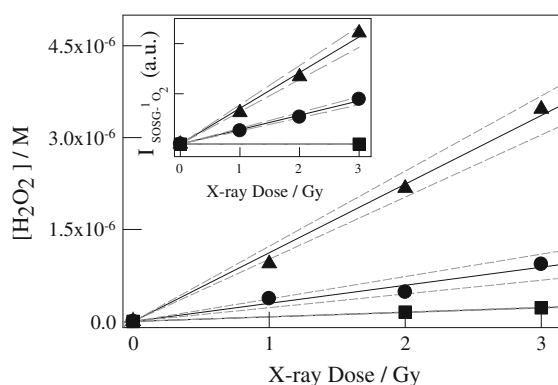


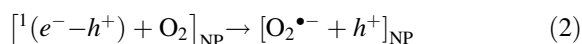
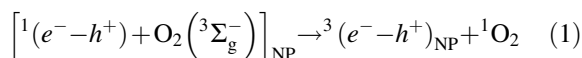
Fig. 5 ROS production in aqueous suspensions: determination of H₂O₂ and ¹O₂. [H₂O₂] formed in X-ray irradiation experiments of aqueous solutions (square), and aqueous suspensions of 0.50 g/L Si-NPC (circle) and 0.50 g/L MMASi-NP (triangle). The symbols size is on the order of the error in the determination of the concentration. *Inset* Fluorescence emission intensity at 525 nm upon 480 nm excitation due to the SOSG-¹O₂ adduct (*I*_{SOSG-¹O₂) in X-ray irradiation experiments of aqueous 5 μM SOSG solutions (square), and 5 μM SOSG aqueous suspensions containing 0.50 g/L of either Si-NPC (circle) or MMASi-NP (triangle)}

the total attenuated radiation is $\sim 11\%$. Therefore, particle attenuation of 4 MeV X-rays is of little significance to account for their 10 to 20 ROS enhancement ratio.

Among the several processes that take place after X-ray attenuation by molecules, Compton scattering is one of the main process at 4 MeV generating photoelectrons and a scattering photon. The energy thus deposited is re-distributed by subsequent interaction of the secondary electrons and photons with the material (Hubbell 1999). High-energy electrons slow down mainly through inelastic collisions with the atoms in materials, creating free radicals. Within such complex

scene, a contributory factor of the presence of the nanoparticles might be the capture and stabilization of the electron as well as the absorption of secondary photons of low energy. Such electrons may also be captured by acceptors in the surface of the nanoparticles, such as adsorbed O_2 leading to $O_2^{\bullet-}$ generation.

Air- and oxygen-saturated aqueous suspensions of MMASi-NP have been reported to produce 1O_2 upon UV-Vis irradiation by a mechanism involving the energy transfer from an exciton $^1(e^-h^+)$ singlet state to surface-adsorbed O_2 (Eq. 1) (Llansola Portolés et al. 2010). Molecular oxygen reduction to $O_2^{\bullet-}$ was proposed (Llansola Portolés et al. 2010) as an alternative decay channel of the nanoparticle singlet spin exciton (Eq. 2). X-ray photon energies are too high to be absorbed in electron transitions yielding excitons, however, their formation by absorption of secondary photons of low energy is a probable reaction path.



In addition, various decay processes may be associated with the dissipation of energy from the high energy hole formed from the excitation of an electron from an occupied orbital of the nanoparticle. In this context, the surface oxidation of the particles to $Si(-O-)_4$ and finally to SiO_2 at the expense of $Si-H$ and $Si-Si$ functionalities may be related to the decay mechanisms of the energetic holes. Moreover, nonadiabatic transitions mediated by surface ligands proposed for the relaxation of semiconductor quantum dot holes (Cooney et al. 2007), may be a possible reaction path generating HO^\bullet radicals from surface silanols. Solution H_2O_2 homolysis due to the high energy radiation may be an alternative source of HO^\bullet radicals.

Nanoparticle uptake and ROS generation by rat glioma C6 cell cultures

Si-NPC uptake by C6 cells was analyzed by spectrofluorometry as described in the experimental section. Figure 6 shows the total Si-NPC fluorescence due to the internalized particles as a function of the incubation time. Internalization of the particles is observed after a lag period of 2 h incubation, reaching a threefold increase after 6 h. Therefore, a 6-h incubation period was employed in all the experiments

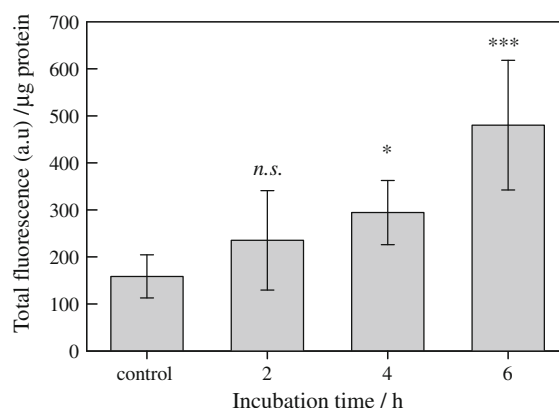


Fig. 6 Nanoparticle incorporation in glioma C6 cells. Total fluorescence intensity of Si-NPC as a function of the incubation time. The data are expressed as mean \pm SD. Experimental differences were analyzed by one-way ANOVA test. Statistically significant differences between controls and experimental groups are indicated by * $p < 0.05$, *** $p < 0.001$, *ns* no significant. Each data is the average of eight replicates

involving C6 cells. Because the nanoparticle luminescence is used as a measure of particle internalization in the cells, this method mainly monitors internalization of Si-NPC of sizes < 5 nm.

In order to gain information on ROS generation by X-ray irradiation of Si-NPC incorporated in C6 glioma cells, irradiation experiments were performed on cell cultures employing the probe CM- H_2 DCF-DA. C6 cells exposed to 50 μ g/mL of Si-NPC for 6 h showed a 36% decrease in cell viability; a further 15% diminution was observed when irradiated with 1 Gy dose of 4-MeV X-rays, lower than the standard dose delivered to the cancer patients (2 Gy). Because the uptake of nanoparticles and X-ray irradiation have an impact on cell viability, C6 cells exposed to 50 μ g/mL of Si-NPC for 6 h were used for ROS generation studies. In fact, concurrent ROS generation assays indicate that the presence of Si-NPC induces ROS generation in the cell, even without radiation as shown in Fig. 7. However, ROS generation increases with the ionizing radiation dose, reaching a 700% at 3 Gy.

Considering that an attenuation coefficient $\mu \sim 0.034 \text{ cm}^{-1}$ is estimated for the cells (Hubbell and Seltzer 2010), while $\mu \sim 0.079 \text{ cm}^{-1}$ is expected for a pure silicon network, the ROS enhancement cannot solely rely on the twofold increase in the X-ray attenuation due to the presence of the silicon particles. As discussed previously, Si-NP interaction with secondary particles and scattered photons might

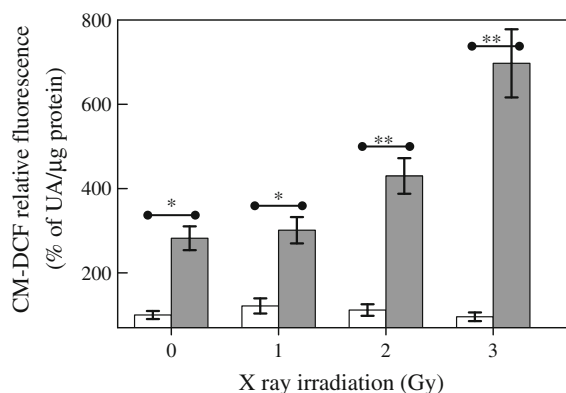


Fig. 7 ROS generation in glioma C6 cells. Relative intensity of CM-DCF fluorescence per μg protein versus irradiation dose for cells incubated in the absence (*white bars*) and in the presence of 50 $\mu\text{g/mL}$ Si-NPC (*gray bars*). The fluorescence intensity of non-irradiated cells in the absence of Si-NPC was taken as 100%. The data are expressed as mean \pm SD. Experimental differences were analyzed by one-way ANOVA test. Statistically significant differences between controls and experimental groups are indicated by * $p < 0.05$, ** $p < 0.001$. Each data is the average of four replicates

induce the generation of ROS. It is well known that induction of excessive ROS generation in the cells promotes mitochondrial membrane permeability and respiratory chain dysfunction triggering different types of cell death (Orrenius 2007). Mitochondrial dysfunction induces the release of electrons from the electron transport chain which in turn causes a second wave of ROS with Complex I and Complex III being sites of $\text{O}_2^{\bullet-}$ generation (St-Pierre et al. 2002).

Interestingly, under our experimental conditions, ionizing radiation is not able to appreciably increase ROS generation in the absence of Si-NPC, see Fig. 7. In this regards, gliomas are highly resistant to ionizing radiation, due to their inability to generate ROS, and/or because of efficient ROS depletion by the cellular antioxidant defense system.

Conclusions

The results obtained in the present study demonstrate that silicon nanoparticles of sizes <5 nm are capable of enhancing the yields of $\text{O}_2^{\bullet-}/\text{HO}_2^{\bullet}$ and HO^{\bullet} in aqueous suspensions as a consequence of X-ray absorption. The concentration of ROS generated upon 4-MeV X-ray irradiation of 6.4 μM MMASi-NP aqueous suspensions were of 10 μM per Gy, one order

of magnitude higher than those obtained in similar experiments in the absence of nanoparticles. Moreover, cytotoxic $^1\text{O}_2$ is formed in irradiated solutions only in the presence of the particles. Singlet oxygen has been reported to be capable of damaging nucleic acids, proteins, and lipids in the cellular environment and has therefore been the subject of intensive research for several decades as the main cytotoxic agent in photodynamic therapy (Dennis et al. 2003). Therefore, silicon nanoparticles capability of producing $^1\text{O}_2$ upon X-ray irradiation opens novel approaches in the design of photodynamic therapy strategies involving ionizing radiation.

Nanoparticle uptake by glioma C6 cells also enhances cellular ROS production, showing a marked increase upon X-ray irradiation, proportional to the radiation dose received. In their absence, no enhanced cellular ROS generation was observed upon X-ray irradiation, confirming the known resistance of C6 cells to ionizing radiation lethal effects.

Silicon nanoparticles have the potential to be used as radiosensitizers for improving the outcomes of existing cancer radiotherapy by employing lower doses of radiation with the consequent decrease in damage to healthy tissue. Specific targeting of the particles to tumor tissues would further potentiate these beneficial properties.

Experimental procedures

Materials

Histidine, phenol, furfuryl alcohol, 2-methyl 2-propanoic acid methyl ester (MMA), toluene, and methanol were all from Sigma-Aldrich (St. Louis, MO). Dimethyl sulfoxide (DMSO) was from Merck (Darmstadt, Germany). Dulbecco's Modified Eagle's Medium with and without phenol red (DMEM-PR and DMEM, respectively) were both from GIBCO BRL, Gaithersburg, MD), amphotericin B and penicillin and streptomycin were from Richet (Argentina) and Rontag (Argentina), respectively. 5-(and-6)-Chloromethyl-2',7'-dichlorodihydro-fluorescein diacetate acetyl ester (CM-H2DCF-DA) was from Invitrogen Molecular Probes (Eugene, OR). Fetal Bovine Serum (FBS) and agarose D1-LE were purchased from Toulbey (Argentina) and Biodynamics Laboratory Inc. (Tokyo, Japan), respectively. Deionized water (>18 M Ω cm, <20 ppb

of organic carbon) was obtained with a Millipore system. Commercially available Si-NPC were from Meliorum Technologies, Inc. (NY, USA). All chemicals were employed without further purification. Toluene [(H₂O 0.005%), 99.7% (GC)], methanol, and MMA were deaerated before synthesis reaction.

Synthesis of MMASi-NP

Silicon nanoparticles were synthesized in the laboratory by the electrochemical etching of porous silicon and derivatized according to previously reported procedures (Llansola Portolés et al. 2009). Briefly, clean crystalline Si wafers (p-type, with resistivity between 1.0 and 10.0 Ω cm) were electrochemically etched (20 mA cm⁻¹ electrical current) in a Teflon cell containing the electrolytic solution (16% HF, 16% CH₃OH v/v). After anodization, the wafer was rinsed with methanol and toluene, further immersed in toluene, and Si-NP released by ultrasound (Ney Dental Inc; 50/60 Hz; 100 W).

Electrochemically synthesized Si-NP were functionalized with 2-methyl 2-propenoic acid methyl ester to avoid further surface oxidation and to stabilize their optical properties, as well as to improve their stability in suspension (Llansola Portolés et al. 2009). Functionalized MMASi-NP were obtained by mixing a colloid dispersion of fresh silicon particles in toluene with 20 μ L of MMA and the resulting suspension irradiated for 20 h with 350 ± 20 nm light from a Rayonet Lamp (RPR 3500 A, Southern N.E. Ultra-violet Co.). MMASi-NP were purified by filtration through hydrophilic 100 nm PVDF membrane filters (MILLEX-HV, Millipore). Membrane filtration was suggested to be an appropriate particle sterilization technique with no significant effect on the particle properties (Ozcan et al. 2009).

The molar MMASi-NP concentration is calculated from the measured w/v ratio taking the number size distribution of the particles, a bulk crystalline silicon density of 2,330 kg/m³ and a SiO₂ monolayer of 2,648 kg/m³ density (Lide 2009). With these considerations, 6.4×10^{-6} mol/L of MMASi-NP are contained in 0.50 g/L suspension.

Nanoparticle characterization

TEM images were acquired using a Philips CM200 UT microscope (point to point resolution 0.19 nm)

operated at 200 kV and room temperature. Samples were prepared by placing drops of the aqueous Si-NPC suspensions on a carbon grid followed by drying at room temperature. Images were analyzed employing the Image Tool 3.0 software (Health Science Center of the University of Texas, San Antonio, USA). Particle diameters were determined assuming that the particle area obtained from the TEM images are the projection of a spherical particle. Dynamic light scattering/static light scattering measurements were performed with a computer controlled BI AT9000 correlator, a BI200SM goniometer (Brookhaven Instruments) and a diode laser ($\lambda = 637$ nm, 5–30 mW power output). Samples were measured at scattering angles of 90°. The temperature of the sample was controlled with a thermostat bath circulator.

Anisotropy time-domain fluorescence experiments were performed with a JOBIN-YVON SPEX FLUOROLOG FL3-11 with LIFETIME TCSPC (time correlated single photon counting) with LED excitation at 341 nm. Experiments were performed for Si-NPC methanol suspensions at 283 K. Fluorescence was detected at 500 nm.

The XPS spectra were obtained under UHV with a XR50 Specs GmbH spectrometer with Mg K α as the excitation source and a PHOIBOS 100 half sphere energy analyzer. Calibration was performed with Au4f 7/2 and Cu2p 3/2 with binding energies of 84.00 and 933.67 eV, respectively. The XPSPEAK-4.1 software was used for the deconvolution of XPS signals. A mixed Gauss-Lorentz (50%) function, a Shirley-type background and a full width at half maximum (FWHM) fixed at 1.4 eV were used for the Si2p signal deconvolution with a spin-orbit doublet separation set at 1.25 eV. The minimum number of components, their binding energies, and peak areas were chosen as those achieving the best adjustment and minimizing random, unstructured residuals.

Optical measurements were performed with aqueous suspensions of the particles at atmospheric pressure and room temperature. Electronic absorption spectra were recorded in a quartz cuvette (1 cm, Hellma) with a Cary 13 UV/Vis double-beam spectrophotometer (Varian, Australia). The scan range was 200–800 nm, with a 300 nm/min rate.

Steady-state luminescent measurements were performed with a Perkin-Elmer LS-50B spectrometer equipped with a Xe lamp as excitation source, a monochromator for selecting the excitation and

emission wavelength (5 nm bandpass gap), and a sensible to the red R928 PMP as detector. All spectra were corrected for the wavelength-dependent sensitivity of the detector and the source by recording reference data simultaneously. Additionally, emission spectra were corrected for Raman scattering by using the solvent emission spectrum. Suspensions of Si-NPC were excited in the range of 220–320 nm and those of MMASi-NP in the 300–400 nm range. The emission spectra were collected in the 350–600 nm range.

The photoluminescence intensity of silicon nanoparticles being a reliable measure of the particles stability in suspension (the reverse statement may not be valid) was routinely checked during the experiments. MMASi-NP aqueous suspensions of pH <6 showed stable luminescence for months (Llansola Portolés et al. 2009, 2010). On the other hand, Si-NPC suspensions exposed to ultrasound previous use showed stable luminescence intensity for 1–2 h. Therefore, stability is not a problem for the aqueous suspensions experiments, though Si-NPC remained aggregated (*vide supra*).

FTIR spectra were obtained with a Bruker EQUINOX spectrometer, with KBr disks as holder. Spectra were taken in the 4,000–400 cm^{-1} with a resolution of 1 cm^{-1} and corrected for the background signal by collecting 64 scans for each measurement. The preparation of the samples involve: the low pressure evaporation of the water solvent, the vacuum-drying of the particle-containing solid residue, mixing of the latter with grounded KBr and pressed into a pellet.

Cell culture and particle uptake determination

Rat glioma C6 cells (ATCC[®] CCL-107TM) were maintained in DMEM medium supplemented with 10% heat-inactivated FBS, 100 U/mL penicillin, 100 $\mu\text{g/mL}$ streptomycin, and 2.5 $\mu\text{g/mL}$ amphotericin B. Cells were cultured on 60-mm plastic dishes at 37 °C under a humidified atmosphere of 5% CO_2 –95% air. For further uses, C6 cells were removed from Petri dishes with 0.25% trypsin, diluted with DMEM/10% FBS and replated.

Si-NPC uptake by C6 cells was determined by spectrofluorometry. Cells were seeded in 12 well-plates at a density of 3.8×10^5 cells/well until 70–80% confluence and then incubated with 0.01 g/L Si-NPC aqueous suspensions for 2, 4, and 6 h. Afterwards, they were washed twice with PBS and

lysed by osmotic shock employing a 7.5 mM KCl solution of pH 7. The lysates were centrifuged at 10,000 $\times g$ for 20 min, and the supernatant fluorescence intensity in the 350–550 nm range monitored upon excitation at 220 nm. The total fluorescence was normalized to the total amount of protein measured by the Bradford's method (Bradford 1976).

For X-ray exposure studies, C6 cells were replated into 96-well plates at a density of 2.8×10^4 cells/well. Cells at a 70–80% confluency were washed with phosphate-buffered saline (PBS) and then used. For experiments with C6 cells containing incorporated nanoparticles, aliquots of a 500 $\mu\text{g/mL}$ aqueous stock Si-NPC suspension were exposed to ultrasound for 2 h, diluted in DMEM/10% SFB to a final concentration of 50 $\mu\text{g/mL}$ and incubated with the cells. After 6 h of incubation, cells were washed twice with PBS, the medium was renewed and cells were irradiated. Cell viability assays were carried out by the neutral red (NR) method based on the incorporation of the NR dye into the lysosomes of viable cells after their incubation with Si-NPC (Babich and Borenfreund 1990; Repetto et al. 2008).

X-ray irradiation

A 4 MeV nominal accelerating potential Varian Clinac electron lineal accelerator was used. The irradiation setup was adjusted for the cell culture to absorb 1–3 Gy, a similar dose to that given to patients under a standard fractionated radiotherapy treatment.

To maintain the electronic buildup, a multiwell acrylic plate system was designed. Central wells were employed for the assays and the two most outer rows and all free spaces were filled with sterile agarose 0.5%. Cells were grown in a monolayer inside acrylic wells covered by 4-mm height of culture medium. The multiwell plate was immersed in a container partially filled with water to fit the height of the culture medium in such a way that the cell layer lies beyond the electronic equilibrium depth when irradiated from below the racket location of the accelerator table. To maintain the electronic equilibrium, experiments employing particle suspensions were performed placing the multiwell plate in a water bath such that the isocenter position is situated 10 cm from the bottom. The dose reaching the sample is 5% lower than the administered value. See ESM 7 for further technical details.

ROS detection and quantification in aqueous suspensions

The global concentration of molecular singlet oxygen ($^1\text{O}_2$), superoxide radicals ($\text{O}_2^{\bullet-}$) and hydroxyl radicals (HO^\bullet) generated upon X-ray irradiation of Si-NP aqueous suspensions were determined measuring the disappearance of selective probes for these species (His, FFA, and PhOH) (Kohn and Nelson 2006). For this purpose, 8 mL aliquots of 0.50 g/L MMASi-NP aqueous suspensions were irradiated in the presence of 1×10^{-4} M of either PhOH, His, or FFA. Taking into account that X-ray water irradiation also leads to the formation of reactive species, residual probes concentrations were also measured in experiments under identical conditions in the absence of particles. The irradiated suspensions were ultracentrifuged for 60 min at 55,000 rpm to separate the particle sediment from the supernatant solution.

The concentrations of PhOH, His, and FFA in the supernatants before and after irradiation were measured by HPLC with a Hewlett-Packard HPLC model 1050 (Ti series) chromatograph with multiwavelength detection, equipped with a C18 Restek Pinacle II column (particle size 5 μm , 2.1 mm i.d. \times 250 mm). Acetonitrile and mixtures of 2 mM formic acid:acetonitrile (95:5) and methanol:water (1:1) were used as eluents for FFA, PhOH, and His, respectively. Under these conditions, up to 0.5 μM concentrations of these compounds were detected.

The probe SOSG was used to specifically detect $^1\text{O}_2$ formation (SOSG, Molecular Probes, Eugene, OR, USA). To that purpose, 8 mL aliquots of 0.5 g/L MMASi-NP or Si-NPC aqueous suspensions were irradiated in the presence of 5 μM of SOSG. The SOSG- $^1\text{O}_2$ adduct formed fluoresces in the green with maximum emission at 525 nm upon 480 nm excitation. To quantify $^1\text{O}_2$ in these experiments, the 525 nm emission was compared to that of the SOSG- $^1\text{O}_2$ adduct formed from a known amount of $^1\text{O}_2$ produced by an identical MMASi-NP suspension when irradiated for 30 min at 360 nm (Llansola Portolés et al. 2009).

The H_2O_2 concentration was measured by an enzymatic colorimetric method employing the commercial Wiener Lab, Argentine kit Colestat for cholesterol quantification. Equal volumes of the irradiated samples and the reagent were mixed and after 30 min of incubation at room temperature, the

absorption spectrum was recorded from 400 to 600 nm. The corresponding calibration curves were performed using standard commercial solutions of H_2O_2 .

ROS generation in cell cultures

ROS production was assessed by an oxidation-sensitive probe, CM-H2DCF-DA (5-(and-6)-chloromethyl-2',7'-dichlorodihydrofluorescein diacetate acetyl ester). In its acetylated form, CM-DCFH2-DA easily crosses lipid membranes and after deacetylation by cellular esterases can be trapped within the cell and oxidized by ROS to form the fluorochrome CM-DCF, which upon excitation at 492–495 nm emits light at 517–527 nm.

CM-H2DCF-DA was dissolved in DMSO and then added to the phenol red-free DMEM culture medium with a final [DMSO] $< 0.1\%$. After irradiation, cells were loaded with a 15 μM CM-H2DCF-DA and incubated for 30 min at 37 °C. Then, cells were washed twice, lysed by osmotic shock and centrifuged as described before. The fluorescence intensity was monitored in the supernatants using a fluorescence plate reader Beckman Coulter-DTX 880 Multimode Detector (excitation and emission wavelengths of 485 and 535 nm, respectively). Cells not exposed to CM-H2DCF-DA were used as a control. Values were normalized to the total amount of proteins.

Acknowledgments This research was supported by the grant PIP 112-200801-00356 from CONICET, Argentina. The authors thank Lic. M. Martinez from the Physical Department at CIO La Plata for his help with the irradiation of the samples, Dr. Aldo Rubbert from INIFTA for the XPS spectrum, B. Soria from CEQUINOR, UNLP for the FTIR spectra, and A. Wolosiuk from CNEA, Bs.As. for the DLS measurements. P.M.D.G. thanks Fundación Avanzar for a postgraduate fellowship. N.I.G. and M.J.L.P. thank CONICET for a studentship. M.C.G. and M.L.K. are research members of CONICET.

References

- Babich H, Borenfreund E (1990) Applications of the neutral red cytotoxicity assay to in vitro toxicology. *ATLA* 18:129–144
- Bertolini G, Coche A (1968) Semiconductor detectors. North Holland Publishing Co., New York
- Bosio GN, David Gara PM, Garcia Einschlag FS, Gonzalez MC, del Panno MT et al (2008) Photodegradation of soil organic matter and its effect on gram-negative bacterial growth. *Photochem Photobiol* 84:1126–1132

- Bradford MM (1976) A rapid and sensitive method for the quantitation of microgram quantities of protein utilizing the principle of protein-dye binding. *Anal Biochem* 72:248–254
- Carter JD, Cheng NN, Qu Y, Suarez GD, Guo T (2007) Nano-scale energy deposition by X-ray absorbing nanostructures. *J Phys Chem B* 111:11622–11625
- Chen M, Mikecz A (2005) Formation of nucleoplasmic protein aggregates impairs nuclear function in response to SiO₂ nanoparticles. *Exp Cell Res* 305:51–62
- Cooney RR, Sewall SL, Dias EA, Sagar DM, Anderson KEH et al (2007) Unified picture of electron and hole relaxation pathways in semiconductor quantum dots. *Phys Rev B* 75:245311
- Dennis EJ, Dolmaris GC, Fucamara D, Jain RK (2003) TIME-LINE: photodynamic therapy for cancer. *Nat Rev Cancer* 3:380–387
- Erogbogbo F, Tien CA, Chang CW, Yong KT, Law WC et al (2011) Bioconjugation of luminescent silicon quantum dots for selective uptake by cancer cells. *Bioconjugate Chem* 22:1081–1088
- Hackley VA, Clogston JD (2007) Measuring the size of nanoparticles in aqueous media using batch-mode dynamic light scattering. NIST-NCL joint assay protocol PCC-1, Version 1.0. http://ncl.cancer.gov/NCL_Method_NIST-NCL_PCC-1.pdf. Accessed 13 July 2011
- Hall EJ, Giaccia AJ (2006) Radiobiology for the radiologist. Lippincott Williams & Wilkins, Philadelphia
- Hubbell JH (1999) Review of photon interaction cross section data in the medical and biological context. *Phys Med Biol* 44:R1–R22
- Hubbell JH, Seltzer SM (2010) Tables of X-ray mass attenuation coefficients and mass energy-absorption coefficients from 1 keV to 20 MeV for elements Z = 1 to 92 and 48 additional substances of dosimetric interest. Ionizing Radiation Division, Physics Laboratory, NIST. <http://www.nist.gov/pml/data/xraycoef/index.cfm>. Accessed 13 July 2011
- Isakovic A, Markovic Z, Nikolic N, Todorovic-Markovic B, Vranjes-Djuric S et al (2006) Inactivation of nanocrystalline C60 cytotoxicity by [gamma]-irradiation. *Biomaterials* 27:5049–5058
- Juzenas P, Chen W, Sun Y-P, Coelho MAN, Generalov R et al (2008) Quantum dots and nanoparticles for photodynamic and radiation therapies of cancer. *Adv Drug Deliv Rev* 60:1600–1614
- Kang Z, Liu Y, Lee S-T (2011) Small-sized silicon nanoparticles: new nanolights and nanocatalysts. *Nanoscale* 3:777–791
- Knoll GF (1989) Radiation detection and measurement. Wiley, New York
- Kohn T, Nelson KL (2006) Sunlight-mediated inactivation of MS2 coliphage via exogenous singlet oxygen produced by sensitizers in natural waters. *Environ Sci Technol* 41:192–197
- Kovalev D, Fujii M (2005) Silicon nanocrystals: photosensitizers for oxygen molecules. *Adv Mater* 17:2531–2544
- Kravets VG, Meier C, Konjhdzic D, Lorke A, Wiggers H (2005) Infrared properties of silicon nanoparticles. *J Appl Phys* 97:1–5
- Lide DR (2009) Handbook of chemistry and physics. CRC Press, Inc., Boca Raton
- Llansola Portolés MJ, Rodríguez Nieto F, Soria DB, Amalvy JJ, Peruzzo PJ et al (2009) Photophysical properties of blue-emitting silicon nanoparticles. *J Phys Chem C* 113:13694–13702
- Llansola Portolés MJ, David Gara PM, Kotler ML, Bertolotti S, San Roman E et al (2010) Silicon nanoparticle photophysics and singlet oxygen generation. *Langmuir* 26:10953–10960
- Mitrasinovic PM, Mihajlovic ML (2008) Recent advances in radiation therapy of cancer cells: a step towards an experimental and systems biology framework. *Curr Radiopharm* 1:22–29
- Orrenius S (2007) Reactive oxygen species in mitochondria-mediated cell death. *Drug Metab Rev* 39:443–455
- Ouyang M, Yuan C, Muisener RJ, Boulares A, Koberstein JT (2000) Conversion of some siloxane polymers to silicon oxide by UV/ozone photochemical processes. *Chem Mater* 12:1591–1596
- Ozcan I, Bouchemal K, Segura-Sanchez F, Abac O, Ozer O, Guneri T, Ponchel G (2009) Effects of sterilization techniques on the PEGylated poly (fA-benzyl-L-glutamate) (PBLG) nanoparticles. *Acta Pharmaceut Sci* 51:211–218
- Park Y-S, Liz M, Kasuya LM, Kobayashi Y et al (2006) X-ray absorption of gold nanoparticles with thin silica shell. *J Nanosci Nanotechnol* 6:3503–3506
- Park J-H, Gu L, von Maltzahn G, Ruoslahti E, Bhatia SN et al (2009) Biodegradable luminescent porous silicon nanoparticles for in vivo applications. *Nat Mater* 8:331–336
- Propst EK, Kohl PA (1994) The electrochemical oxidation of silicon and formation of porous silicon in acetonitrile. *J Electrochem Soc* 141:1006–1013
- Repetto G, del Peso A, Zurita JL (2008) Neutral red uptake assay for the estimation of cell viability/cytotoxicity. *Nat Protoc* 3:1125–1131
- Ross AB, Mallard WG, Helman WP (1998) NDRL-NIST solution kinetics database: Ver. 4.0. <http://kinetics.nist.gov/solution/>. Accessed 13 July 2011
- Ryckman JD, Reed RA, Weller RA, Fleetwood DM, Weiss SM (2010) Enhanced room temperature oxidation in silicon and porous silicon under 10 keV X-ray irradiation. *J Appl Phys* 108:113528–113534
- Schärtl W (2007) Light scattering from polymer solutions and nanoparticle dispersions. Springer, Berlin
- Seino S, Yamamoto TA, Hashimoto K, Okuda S, Chitose N et al (2003) Gamma-ray irradiation effect on aqueous phenol solutions dispersing TiO₂ or Al₂O₃ nanoparticles. *Rev Adv Mater Sci* 4:70–74
- Soffietti R, Leoncini B, Rudà R (2007) New developments in the treatment of malignant gliomas. *Expert Rev Neurother* 7:1313–1326
- St-Pierre J, Buckingham JA, Roebuck SJ, Brand MD (2002) Topology of superoxide production from different sites in the mitochondrial electron transport chain. *J Biol Chem* 277:44784–44790
- Takahashi J, Misawa M (2007) Analysis of potential radiosensitizing materials for X-ray-induced photodynamic therapy. *NanoBiotechnology* 3:116–126
- Wang PW, Bater S, Zhang LP, Ascherl M, Craig JH (1995) XPS investigation of electron beam effects on a trimethylsilane dosed Si(100) surface. *Appl Surf Sci* 90:413–417
- Wang L, Yang W, Read P, Larner J, Sheng K (2010) Tumor cell apoptosis induced by nanoparticle conjugate in

- combination with radiation therapy. *Nanotechnology* 21:475103–475110
- Yang CS, Oh KS, Ryu JY, Kim DC, Shou-Yong J et al (2001) A study on the formation and characteristics of the Si–O–C–H composite thin films with low dielectric constant for advanced semiconductor devices. *Thin Solid Films* 390: 113–118
- Yang W, Read PW, Mi JM, Baisden JM, Reardon KA et al (2008) Semiconductor nanoparticles as energy mediators for photosensitizer-enhanced radiotherapy. *Int J Radiat Oncol* 72:633–635
- Yoffe AD (2001) Semiconductor quantum dots and related systems: electronic, optical, luminescence and related properties of low dimensional systems. *Adv Phys* 50:1–208
- Zhang XD, Guo ML, Wu HY, Sun YM, Ding YQ et al (2009) Irradiation stability and cytotoxicity of gold nanoparticles for radiotherapy. *Int J Nanomed* 4:165–173